Spin Crossover-assisted modulation of electron transport in a single crystal 3D metal-organic framework

Ana Martinez-Martinez,[a] Esther Resines-Urien,[a] Lucía Piñeiro-López,[a] Angel Fernández-Blanco,[b,c] Antonio Lorenzo Mariano,[c] Jorge Albalad,[d,e] Daniel Maspoch,[d,e,f] Roberta Poloni,[c] Jose Alberto Rodríguez-Velamazán,[b] E. Carolina Sañudo,[g,h] Enrique Burzurí,*[a,i] and José Sánchez Costa*[a]

[a]IMDEA Nanociencia, C/ Faraday 9, Ciudad Universitaria de Cantoblanco, 28049 Madrid, Spain

[b]Institut Laue-Langevin, 6 rue Jules Horowitz, BP 156, 38042 Grenoble Cedex 9, France

[c]Univ. Grenoble Alpes, CNRS, SIMAP, Grenoble, 38000, France

[d]Catalan Institute of Nanoscience and Nanotechnology (ICN2), CSIC and The Barcelona Institute of Science and Technology, Campus UAB, Bellaterra, 08193 Barcelona, Spain

[e]Departament de Química, Facultat de Ciències Universitat Autònoma de Barcelona, 08193 Bellaterra, Spain

[f]ICREA, Pg. Lluís Companys 23, 08010 Barcelona, Spain

[g]Departament de Química Inorgànica i Orgànica, Secció de Química Inorgànica, Universidad de Barcelona, C/Martí i Franqués 1-11, 08028 Barcelona, Spain

[h]Institut de Nanociència i Nanotecnologia, Universitat de Barcelona (IN2UB), C/Martí i Franqués 1-11, 08028 Barcelona, Spain

[i]Departamento de Física de la Materia Condensada and Condensed Matter Physics Center (IFIMAC), Universidad Autónoma de Madrid, 28049 Madrid, Spain

Email corresponding author(s): enrique.burzuri@imdea.org ; jose.sanchezcosta@imdea.org

ABSTRACT: Molecule-based Spin Crossover (SCO) materials display likely one of the most spectacular switchable processes. The SCO involves reversible changes in their physicochemical properties (i.e. optical, magnetic, electronic and elastic) that are coupled with the spin-state change under an external perturbation (i.e. temperature, light, magnetic field or the inclusion/release of analytes). Although very promising for their future integration into electronic devices, most SCO compounds show two major drawbacks: i) their intrinsic low conductance, and ii) the unclear mechanism connecting the spin-state change and the electrical conductivity. Herein, we report the controlled single-crystal-to-single-crystal temperature-induced transformation in a robust metal-organic framework (MOF), $[Fe_2(H_{0.67}bdt)_3]\cdot 9H_2O$ (**1**), being bdt^{2-} = 1,4-benzeneditetrazolate, exhibiting a dynamic spin-state change concomitant with an increment in the anisotropic electrical conductance. Compound **1** remains intact during the SCO process even after approximately a 15 % volume reduction. The experimental findings are rationalized by analyzing the electronic delocalization of the frontier states by means of density-functional theory calculations. The results point to a correlation between the spin-state of the iron

and the electronic conductivity of the 3D structure. In addition, the reversibility of the process is proved.

INTRODUCTION

The future of electrically conducting materials is moving apart from the current design-limited metal-oxide semiconductors technology. In this perspective, three-dimensional metal-organic frameworks (MOFs)[1,2] containing transition metals have been proposed as an elegant synthetic strategy to achieve novel electrically conducting materials.[3,4] Although this research is still in its infancy, mainly due to the low conductivity nature of these materials, some strategies[5] are critically improving electron transport reaching conductivities comparable to that of graphene.[6] Some of these strategies involve stronger charge delocalization between metals and ligands,[7] the introduction of π-π continuous charge transport pathways,[8] extended conjugation through the organic framework[6,9–11] and, uniquely in MOFs, transport mediated through guest molecules.[12–14] Recently, it has been established that not only the design of the framework determines the conductance in the MOF but also the selection of the metal is critical to obtain non-negligible conductance through an otherwise equivalent MOF.[15,16] In particular, iron seems to be the best candidate to obtain high-conductance MOFs.

Besides conductivity, MOFs are as well significantly versatile materials to host magnetism.[17,18] Magnetic centers can be introduced in different positions of the ordered lattice, from the coordination framework[17] to the inorganic nodes[19] and as guest molecules[20,21] to provide MOFs with magnetic order[22,23] or single molecule magnetism (SMM)[24,25] that could be used for quantum

bits,[26] in spintronics[27] and likely in one of the most spectacular switchable behaviors, the spin crossover (SCO) phenomenon.[28,29]

Fe(II) is likely the most studied magnetic cation in the SCO family because of the drastically different properties between its High Spin (HS, S = 2, paramagnetic) and Low Spin (LS, S = 0, diamagnetic) states.[30–32] Occasionally, the balance between these two states is so delicate that modulation of an external parameter is sufficient to reversibly switch between them. This external perturbation induces the so-called SCO between HS and LS states (**Figure 1a**).[33] Although temperature is the most common method to switch between the spin states, it can also be achieved through light irradiation,[34,35] pressure[35] or the inclusion/exclusion of small molecules into the material, including water molecules, as described here.[36–38] The SCO transition also causes a variation of ≈ 12 % of the metal-to-ligand bond distances (**Figure 1a**) leading to a remarkable change of molecular size and shape during the spin conversion. Notably, in the solid state, the SCO always involves a structural transformation in the material, concomitant with different magnetic, optical, electrical, and structural outputs.[39]

The combination of electrical conductivity and the SCO phenomenon in a single material has been a long-desired goal of the scientific community or even further, a "scientific dream"[40] since the electrical current would constitute a more viable way to read signals in SCO devices. There is experimental evidence that the spin-state switching may lead to a reversible increase/decrease of the electrical conductance and dielectric constant in the SCO material, making SCO compounds ideally suitable for the construction of electronic devices[4,41–44] However, the actual exploitation of the SCO is a challenge[45] since SCO materials are insulating by nature. To surpass this critical drawback three main strategies are pursued i) design of devices in which the spin change of the

metal centers is reflected in the electrical signal of a conductor;[46–48] ii) morphology control and

SCO particle-size reduction[49–51] and iii) promote conductivity in the bulk material (powders and

single crystals).[52–55] Thus, the electronic charge transport study and its interplay with

magnetically active spin-state switch is very attractive and remains challenging, mainly due to

the difficulty of obtaining both properties in a single crystalline material. In this work, we

explore the relationship between the conductivity variation and the electronic (and spin) state in a

single crystal MOF.[4]

With these considerations in mind, we chose to study the robust framework

$[Fe_2(H_{0.67}bdt)_3] \cdot 9H_2O$ (**1**) (**Figure 1**), being bdt^{2-} = 1,4-benzeneditetrazolate (**Figure 1b**),[56,57] that

undergoes a partial SCO transition at low temperature. Sample **1** is built via tetrazolate-bridged

1D chains of Fe(II) forming a triangular three-dimensional structure with a large surface area

(**Figure 1c,d**).[13] We note that a polymorph of this framework exhibiting Fe(III) defects has been

reported by Long and Dincă et al. to provide the highest conductance ever reported in MOFs.[58]

Therefore, this MOF combines the main ingredients to be magnetically active and, at the same

time exhibits a significant conductance owing to the interplay between the metal centers, the

pyrazolated groups and the guest water molecules.

Here, we report the controlled single-crystal-to-single-crystal temperature-induced

transformation from $[Fe_2(H_{0.67}bdt)_3] \cdot 9H_2O$ (**1**) to $[Fe_2(H_{0.67}bdt)_3] \cdot 4H_2O$ (**2**) and

$[Fe_2(H_{0.67}bdt)_3] \cdot 2H_2O$ (**3**). Exceptionally, the Fe(II) MOF crystallinity remains intact in **2** and **3**

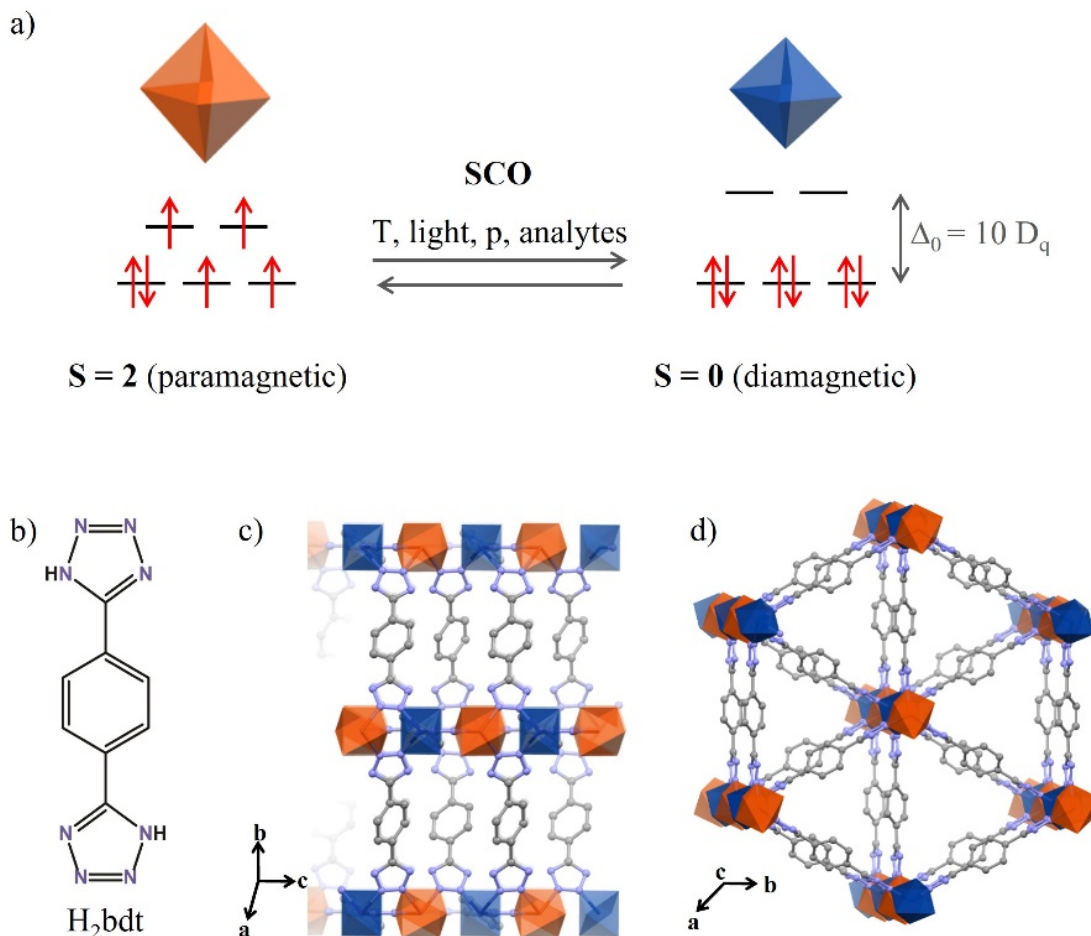even after approximately a 15 % volume reduction.

Figure 1. (a) Representation of the two spin states of an ion with six *d* electrons, the high-spin (HS, paramagnetic) and the low-spin (LS, diamagnetic) electronic states. Under external stimuli, such as temperature, pressure, light irradiation, or the inclusion of analytes, the crystal field splitting Δ_0 can be modified and the SCO materials can switch between both electronic states. (b) H_2bdt ligand drawing. (c) 1D Fe(II)-tetrazole building block and view of the layer formed from the 1D chains. (d) 3D perspective of **1**. LS Fe is represented in dark blue, HS Fe in orange, N in blue and C in grey.

Furthermore, the **1→2→3** crystal transformation exhibits a dynamic spin-state change concomitant with an increment in the anisotropic electrical conductance. The theoretical rationalization of experimental results by means of the analysis of the electronic structure in the

MOF points to a correlation between the spin-state of the iron and the electronic conductivity of the 3D structure. In addition, the reversibility of the process (**3→1**) is proved by powder X-ray diffraction (PXRD).

EXPERIMENTAL SECTION

All reagents and solvents were commercially available and used as received. The $FeSO_4$ was purchased from Scharlab while the precursors of the H_2bdt ligand and the NaSCN were purchase from Fluorochem. The H_2bdt ligand and the MOFs **1**, **2** and **3** were synthesized using a method reported in the literature[56,59] with modifications (details in the **ESI†**). FT-IR spectra were recorded as neat samples in the range 400-4000 cm^{-1} on a Bruker Tensor 27 (ATR device) Spectrometer. TGA was performed using a TA Instrument TGAQ500 with a ramp of 1 °C min^{-1} under air from 303 to 873 K. Optical reflectivity measurements between 288 and 373 K were performed using a MOTIC SMZ-171 optical stereoscope coupled with a MOTICAM 3. Images were collected in BMP format without any filter using the Motic Images Plus 3.0 software, with the mean value from each region of interest (ROI) analyzed under the ImageJ program. The temperature was controlled using a Linkam T95 system controller and a LNP 95 Liquid Nitrogen Cooling System. NMR spectra were recorded on a Bruker Advance 300 (1H: 400 MHz) spectrometer at 298 K using partially deuterated solvents as internal standards. Elemental analysis (C, H and N) was performed on a LECO CHNS-932 Analyzer at the "Servicio Interdepartamental de Investigación (SIdI)" at Autónoma University of Madrid. Differential Scanning Calorimetry (DSC) measurements were performed in a Setaram DSC-131 calorimeter between 298K and 470 K at a heating rate of 10 K/min. For this experiment, 1.5 mg of sample were used, and blank runs were performed. Powder X-ray diffraction (PXRD) measurements

were collected on a Panalytical X'pert MPD diffractometer with monochromatic Cu-Kα radiation (λCu = 1.5406 Å) equipped with a capillary stage and operating under transmission mode. Solid samples of **1**, **3**, and **1'** were mounted and flame sealed within Pyrex® capillary tubes (Øint = 0.7 mm) prior to PXRD measurements. DC electron transport measurements were carried out on single crystals of **1** by a two-probe method using a Keithley 2450 SourceMeter under light. Electrical contact to individual **1** crystals are made directly via the conducting tips of the electrical probe station. Charge transport is probed along the ab plane of the crystals. The length of the crystals and the separation between the tips is typically a few hundred micrometers (100-200µm). The temperature was controlled using a Linkam T95 system with a LNP 95 Liquid Nitrogen Cooling System. AC admittance spectroscopy measurements were performed in a Lakeshore Cryogenics (Model PS-100 Tabletop) probe station, equipped with a Zurich Instruments MLI500 kHz Lock-in-Amplifier. Measurements were carried out with a heating rate of +2 K·min^{-1} and AC excitation frequency: $\omega/2\pi$= 10 kHz; AC voltage Vac = 100 mV; offset DC bias voltage: V = 1 V). DFT calculations were performed using QuantumEspresso.[60,61] The structural optimization of **1** and **3** is performed for the bare materials without water molecules using the PBE functional in conjunction with the optimized norm-conserving Vanderbilt pseudopotentials.[62] The projected band structure and electronic density of states are computed using the PBE+U approach.[63] In order to achieve a good description of the electronic structure of Fe (II) complexes using the Hubbard U method,[64,65] we have parametrized U for all the atoms of the primitive cell in order to mimic the density of states obtained using the well-behaved Heyd–Scuseria–Ernzerhof (HSE) exchange-correlation functional functional.[66,67] Additional technical

details regarding the calculations and the comparison of PBE+U with other functionals are reported in the **ESI**†.

RESULTS AND DISCUSSION

Magneto-structural temperature-induced transformation of [Fe$_2$(H$_{0.67}$bdt)$_3$]·9H$_2$O (1)

Orange hexagonal single crystals of **1** were obtained by slightly modifying the method reported by Dan Li et al.[56] (see **Figure 1** and **ESI**† for further details). Single crystal X-ray diffraction analysis at 300 K reveals that compound **1** presents an incommensurate modulated structure, with superstructure reflections appearing in the c-direction. The fundamental reflections correspond to a hexagonal unit cell $a, b = 22.59(3)$ Å, $c = 7.46(3)$ Å, as seen in **Table S1**†, while the superstructure reflections can be indexed by multiplying the c-axis of the basic cell by a factor of ca. 4. The modulated structure is most probably due to a positional disorder of the tetrazole ligands propagating along the c-direction. To avoid the complexity of such description and to facilitate comparison, we described an average structure in the basic unit cell, keeping only the fundamental reflections and modelling the actual position of the tetrazole by a disorder of the molecule in three positions. This basic structure can be described in the trigonal space group $R\overline{3}$.

The asymmetric unit contains two crystallographic independent Fe(II) metal centers and three H$_2$bdt ligands (details of the structure solution and refinement are summarized in **Table S2**†). Both iron metal centers show an octahedral environment in which they are coordinated to six

nitrogen atoms belonging to six different H_2bdt ligands defining {Fe-(tetrazolate)}$_n$ chains. The average Fe-N bond lengths are Fe1-N1: 1.972 Å and Fe2-N2: 2.182 Å (**Table S3†**), i.e. Fe1 is in the range of low spin-state while Fe2 is in the high spin-state.[68] The three-dimensional structure is expanded along the c axis, where one-dimensional Fe-tetrazole chains are linked by 2,3-bridging tetrazole of three different H_2bdt ligands (**Figure 1c**).[56,57] The octahedral sequential orientation gives rise to an overall zig-zag distribution along the *c*-axis (**Figure S5†**). The cell parameters were monitored to follow the evolution of the crystalline structure of **1** with temperature. As can be noticed, the structure evolves with temperature, with two very noticeable changes mainly in the periodicity along *c* as deduced from the superstructure reflections. The first change occurs around 320-330 K and the second one above 380 K (**Figure 2**). A crystallographic study was performed at three specific temperatures, i.e. before the first abrupt change in the periodicity along *c*, at 300 K (**1**), right before the second notable change, at 353 K (**2**), and after the last change at 420 K (**3**) (**Figure 3a** and **ESI†**).
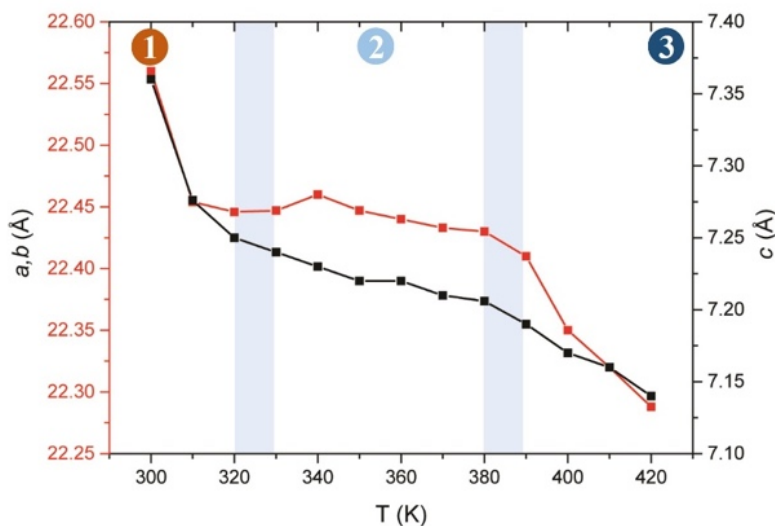
Figure 2. Evolution of the cell parameters with the temperature. The data extracted from SCXRD is given in **Table S1**†

Single crystal X-ray diffraction analyses reveal that **2** and **3** crystallize in the trigonal space groups *R3m* and *R$\overline{3}$m*, respectively. Similarly to **1**, phases **2** and **3** contain two independent Fe(II) centers octahedrally coordinated to six H_2bdt ligands. However, in **2**, a decrease in the metal-donor bond lengths is observed (Fe1-N: 1.926 Å, Fe2-N: 1.995 Å, see **Figure 3a** and **Table S3**†). These Fe-N distances correspond to both Fe(II) atoms in the LS state.[69] The spin transition from HS to LS in the Fe(II) centers occurs concomitantly with the loss of water molecules as the temperature is increased (see **SI**† for further details). In **3**, the Fe-N distances are reduced even further, in accordance with both Fe(II) metal centers in the LS state (Fe1-N1: 1.912 Å, Fe2-N2: 1.975 Å). Regarding the distances between the metal centers, a decrease is observed as the temperature increases. The Fe1-Fe2 distances are 3.732 Å, 3.588 Å and 3.540 Å along the *c* axis and 13.103 Å, 12.883 Å and 12.856 Å in the plane *ab*, respectively for **1**, **2** and **3** (**Figure S6**†).
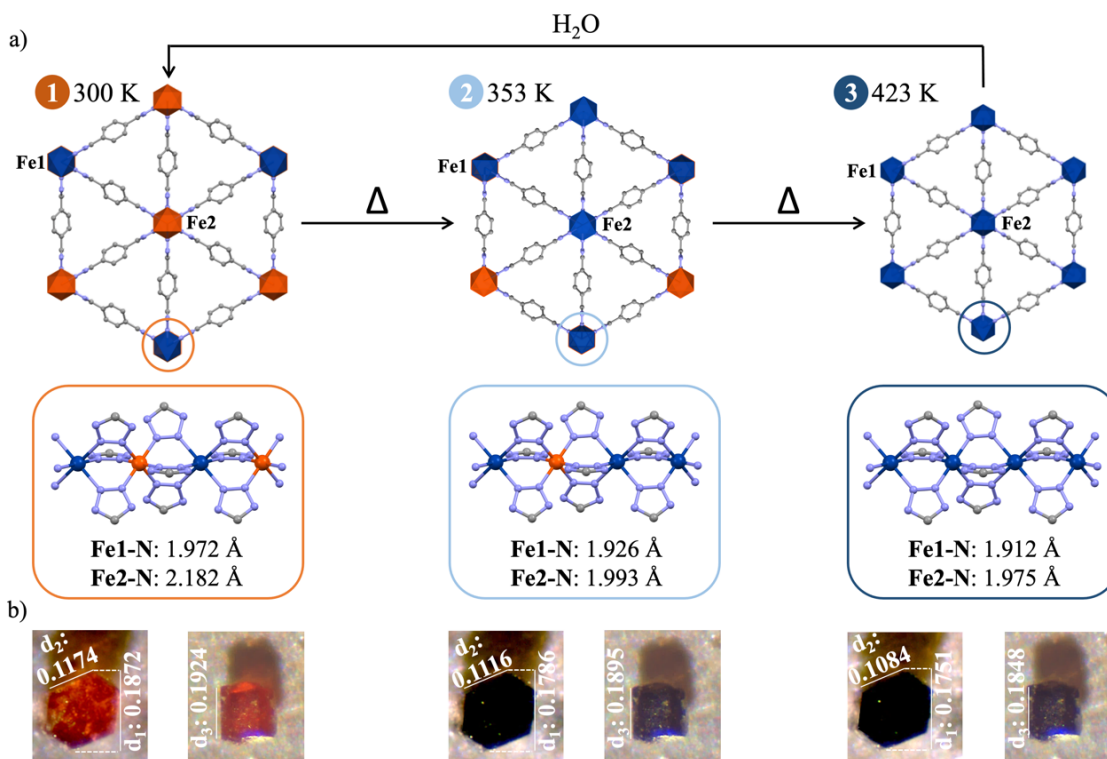
Figure 3. (a) Crystal structures of **1**, **2** and **3**, where LS Fe is represented in dark blue, HS Fe in orange, N in blue and C in grey. The disorder of the tetrazole molecules and H atoms have been omitted for clarity. Fe-N distances are given in Å. The reversibility methodology from **3** to **1** is explained in detail in the SI. (b) Optical images of **1** at room temperature, **2** after heating up to 353 K and **3** to at 423 K and subsequent change of color and length (in mm) in plane *ab* (d_1 and d_2) and in the *c* axis (d_3).

Spin crossover materials are quite sensitive to the presence/absence of guest molecules,[70] like water.[28,71] A thermogravimetric analysis (TGA) was performed from room temperature up to 873 K (see **Figure S7†**). A first weight loss begins at around 305 K and ends at 350 K (10.14 %) suggesting the loss of five water molecules which gives rise to $[Fe_2(H_{0.67}bdt)_3] \cdot 4H_2O$ (**2**). A second change in the slope around 350 K and 423 K (3.57 %) fits with the release of two additional water molecules, coinciding with the novel formulation $[Fe_2(H_{0.67}bdt)_3] \cdot 2H_2O$ (**3**).

Following the 1→2→3 transformation

The SCO switch suggested by the change in the Fe-N distances was confirmed by measuring the magnetic susceptibility, χ_M, of the crystals in the 10 K to 375 K temperature range, which is covering the **1** and **2** phases of the crystal (**Figure 4a**). At room temperature, the $\chi_M T$ value is 3.18 cm^3 K mol^{-1}, a value in agreement with two independent Fe(II) sites, one in HS state and the other in LS state. Upon cooling **1** to 20 K, the $\chi_M T$ value decreases attaining a value of 2.3 cm^3 K mol^{-1}, corresponding to the transition of approximately 30 % of the Fe(II) ions in HS state into LS, with a transition temperature $T_{1/2}$ of 125 K.[56,57] Upon heating the sample back to room temperature, the magnetic susceptibility reaches the starting $\chi_M T$ value of 3.18 cm^3 K mol^{-1}. Interestingly, when **1** is heated up to 353 K and therefore to the **2** crystalline phase, $\chi_M T$ decreases abruptly to reach 1.89 cm^3 K mol^{-1} which is consistent with 70 % of the Fe(II) ions being in the LS state (**Figure 3a**). The maximum temperature that could be reached in the SQUID magnetometer used for this measurement was 375 K, at which a value of 1.33 cm^3 K mol^{-1} was obtained. This corresponds to 80 % of the metal centres in the LS. Based on values of Fe-N distances obtained in SCXRD (**Table S3†**) and this trend of decreasing $\chi_M T$ with temperature, everything indicates that at 423 K (**3**) all Fe(II) ions are in LS at 423K (**3**).

The spin transition in the crystals is accompanied by a clear color change of the material from orange to dark blue (**Figure 3b**). To obtain additional information on the variation of this optical property with temperature, optical reflectivity measurements were performed. The optical reflectivity (O.R.) of an orange crystal of **1** measured while heating it from 298 K to 480 K is shown in **Figure S8†**. Initially, as the temperature increases, the O.R. decreases progressively mirrored by a darkening of the crystal. When the temperature reaches 340 K, the crystal turns to

a dark blue color until 370 K. In addition to the color change, a volume variation in the crystals can be seen as the temperature increases. Thereby, three different distances *i.e.* d_1 and d_2 in the *ab* plane and d_3 coincident with the *c* axis were measured in five crystals (**Figure S10†**). The data obtained, compiled in **Table S4†**, allowed us to calculate the percentage of reduction (%) in the three distances with increasing temperature when going from **1** to **3** by increasing the temperature, obtaining that the crystals size decreases an average of 6.2 ± 0.3 % in d_1, 7.2 ± 0.4 % in d_2 and 3.8 ± 0.8 % in d_3. Therefore, the relative crystal volume reduction, assuming that the crystals are regular hexagonal prisms, is 15.8 ± 0.9 % (**Figure S11†**).

Water molecules are therefore clearly evacuated from the pores of the three-dimensional lattice with increasing temperature. A control test was carried out to establish whether the undergoing spin transition is induced by temperature or by the loss of water molecules. Thus, some crystals of **1** were immersed in oil and others were left in the air. The temperature was gradually increased, and it was observed that the color change of the crystals in air occurred at much lower temperature (323 K) than in the crystals immersed in oil (348 K) (**Figure S9†**), confirming the direct link between the loss of water molecules and the spin transition. This could be related with the mobility of the aromatic rings in the structure which is higher as the hindrance provided by the water molecules is removed. A similar mechanism was previously observed in other porous SCO compounds.[72]
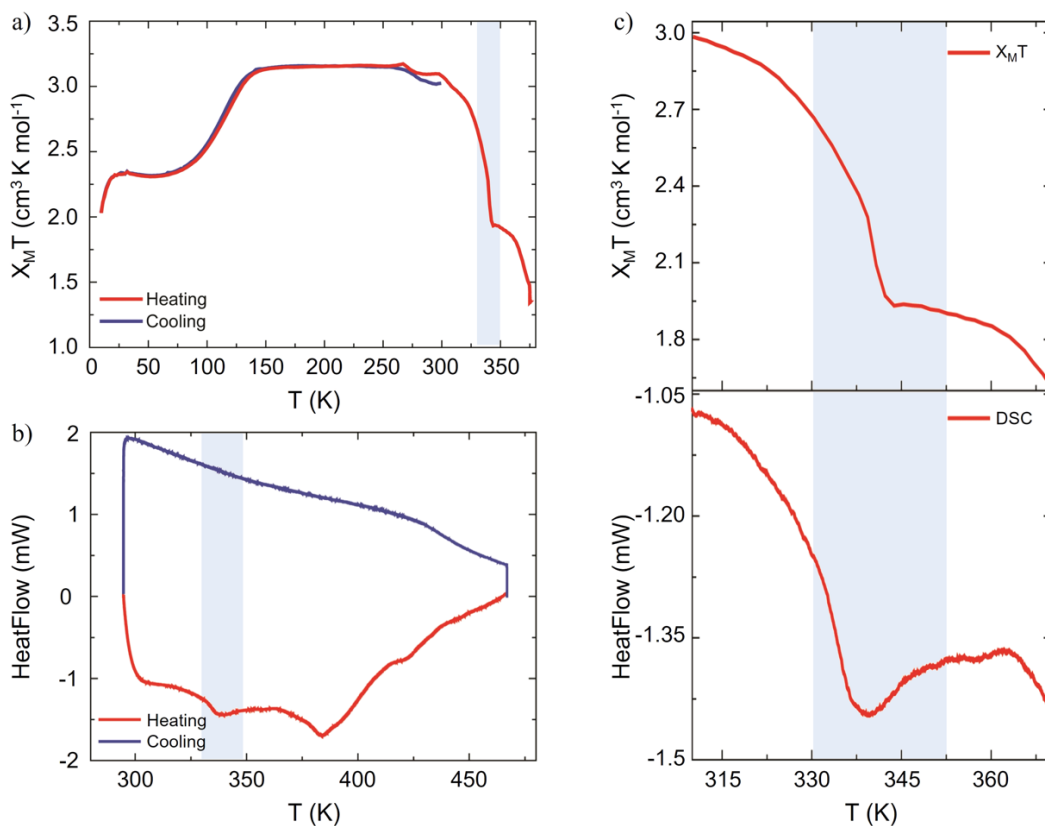
Figure 4. (a) Differential scanning calorimetry between 298 K and 480 K. (b) Temperature dependence of X_MT. (c) Zoom of the DSC and X_MT plot between 300 and 375 K.

To obtain further evidence of the two magneto-structural transitions in **1**, differential scanning calorimetry (DSC) measurements were performed between 293 K and 473 K. Two endothermic peaks, *i.e.* the crystal absorbs energy, can be observed during the heating process (**Figure 4b**). The first one is centered around 337 K and is consistent with the structural changes and the first magnetic transition described (**Figure 4c**). In addition, a second endothermic peak is observed around 383 K in agreement with a second abrupt change in the periodicity along the cell parameters.

Reversibility

Powder X-ray diffraction (PXRD) measurements of the hydrated (**1**), dehydrated (**3**) and rehydrated (**1'**) forms were carried out to study the reversibility of the process. The results are shown in **Figure S12**†. The patterns obtained from polycrystals **1** and **3** are in excellent agreement with the simulated single-crystal diffractograms.

Sample **1** was heated for 12 hours at 423 K under vacuum to ensure that H_2O molecules were completely desorbed from the material. The PXRD was then performed. The first observation is that the pattern collected is different from the previously collected for **1**. The appearance/shift of the peaks suggests a new crystalline phase associated with the evacuation of H_2O molecules. Comparison of this pattern with that simulated for single crystal of **3** confirms that they are in the same crystallographic phase. Afterwards, **3** was immersed in H_2O for 6 hours giving rise to the rehydrated form, named **1'**. The diffractogram suggests that **1'** is the same as **1**, in agreement with the reversibility of the process.

Electron transport measurements of 1→2→3

Based on the previously reported high conductivity of an isostructural MOF,[13] charge transport across individual crystals of **1** was explored to understand the impact that the sharp structural and magnetic transformation in the MOF may have on its electronic properties. Thereby, the electrical current (*I*) was measured by making direct contact with individual crystals in an electrical probe station, as shown in **Figure 5a**. The crystal color evolution with temperature is consistent with that observed in the reflectivity measurements, confirming that the structural transitions are preserved in this setup throughout high electrical fields in the charge transport measurements.

Figure 5b shows the current-voltage (*IV*) characteristics measured on a single crystal between 298 K and 423 K. The tips of the probes are connected to the lateral facets of the hexagons so that charge transport is mainly probed along the *ab* crystallographic plane (see **Figure 1a**). The current shows a non-linear, asymmetric dependence with bias, probably indicating the presence of Schottky barriers at the interface between electrodes and the material and/or between grain boundaries in the crystal.

The main *IV* characteristics are roughly reproducible in all the measured crystals (example shown in **Figure S14†**). Remarkably, the current monotonously increases from around 10^{-10} A at room temperature to 10^{-8} A at 423 K, *i.e.* two orders of magnitude difference. The conductivity at the highest temperatures reaches $\sigma = (6.1 \pm 0.2) \cdot 10^{-8}$ S cm^{-1} (**Figure S15†** and **Table S6†**). This value is comparable to those found in the literature for other Fe-based MOFs at room temperature[15] and larger than those found in other metal MOFs.[3] Note that the complex crystal shape together with its continuous change in volume makes it difficult to estimate its effective dimensions (see **Table S4†**). This high-conductance can be expected for Fe-MOFs linked by tetrazolates, where the azolate tends to promote electronic coupling between the metals and the organic framework.[3,13] In addition, the H_2bdt bridge linking different chains is conjugated, contributing to the delocalization and mobility of the electrons. A similar increment of the current with temperature is observed when *I* is measured at a fixed bias voltage (*V* = 4 V), as seen in **Figure 5c**. The current grows exponentially with temperature, indicative of thermally activated transport across the crystal. Interestingly, three distinct regions can be roughly distinguished in temperature that could correspond to the three magneto-structural metastable states described for this MOF.
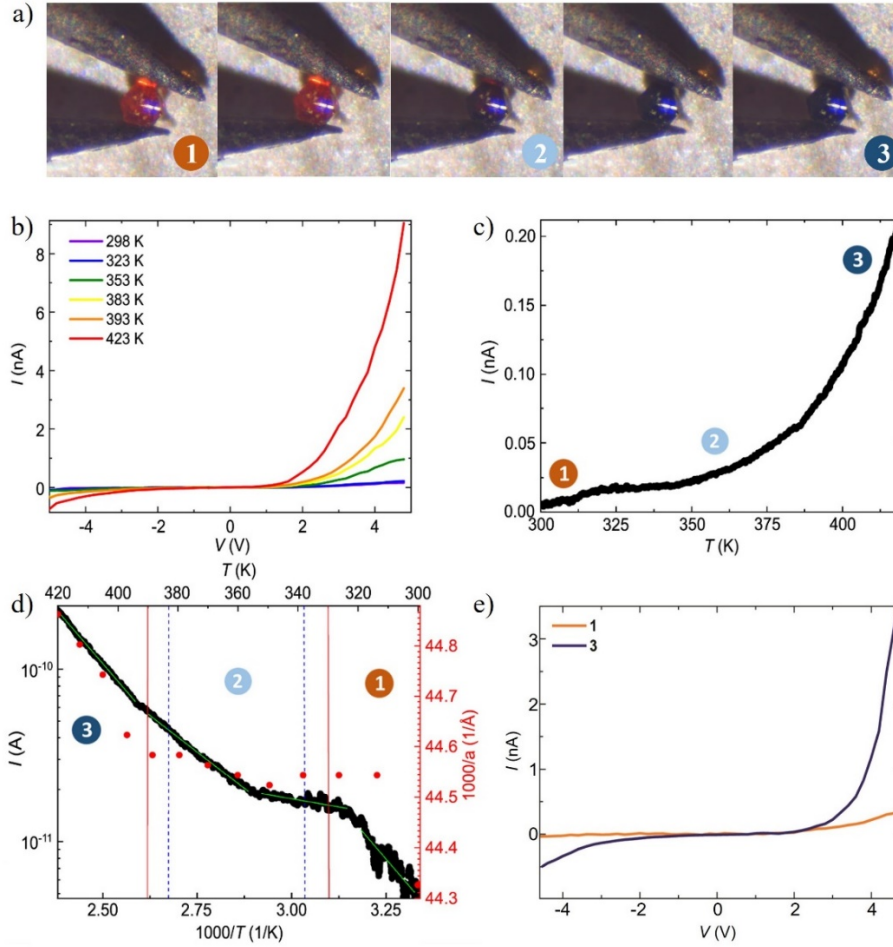
Figure 5. (a) Optical images of a single crystal trapped between the conducting tips of an electrical probe station. The numbers indicate the different crystal states shown in **Figure 2**. (b) Current-voltage *IV* characteristics measured on a single crystal at different temperatures. (c) *I* measured as a function of T at a fixed *V* = 4 V. Three different regions (marked **1**, **2** and **3**) can be observed at temperatures consistent with the magneto-structural transitions. (d) Arrhenius plot of the measurement in (c). The vertical lines mark the structural transitions observed in the DSC (blue dotted lines) and in the X-ray diffraction (red solid lines) experiments. The green lines are fits to an Arrhenius law with activation energy barriers: 220 meV, 33 meV, 146 meV and 219 meV from low to high temperatures. The red dots represent the inverse lattice parameters *a*, *b* as a function of the temperature. (e) Current-voltage *IV* characteristic measured at

18

room temperature in **1** and the same crystal after ramping up to 423 K (transformation to **3**) and cooling down back to room temperature. The larger conductance in **3** is preserved even at room temperature.

Figure 5d shows the Arrhenius plot of the same measurement. The vertical lines mark the structural transitions observed in the DSC and magnetic measurements (blue dotted lines) and in the X-ray diffraction (red solid lines) experiments. The distinct temperature regions are clearly observed and approximately fit between the structural transitions. The solid green lines are fits to an Arrhenius law in the corresponding temperature ranges. The activation energies (E_a) obtained from the fits are 220 meV, 33 meV, 146 meV and 219 meV from low to high temperature respectively. These values are in line with those reported in literature for highly conducting MOFs.[15,58]

The switch in the activation energy seems therefore intrinsically related to the magneto-structural changes in the crystal. This scenario is reinforced by directly comparing *I* with the change in the *a, b* lattice parameters with temperature (red dots in **Figure 5d**). Current and lattice parameters (directly connected to the SCO transition and the spin-state) qualitatively follow the same trend with temperature. Interestingly, in spite of some controversy in the field, many reports in literature show that SCO crystals in their LS state are more conducting that in the HS state,[4] although this may be very sensitive to the local environment at the nanoscale.[73] It seems therefore that the SCO transition could be behind the sharp reduction of E_a (from 220 meV to 33 meV at around 330 K), observed in **Figure 5d**. The subsequent increment in E_a could be associated with the second structural transition and the progressive change in the lattice parameters. This scenario is further supported by impedance spectroscopy measurements shown in **Figure S17†,** that in addition show the high-quality crystallinity of the samples, in all

temperature range (from **1** to **3**). Remarkably, the increment in the conductance observed in **3** is preserved when cooling down the crystal back at room temperature, as seen in **Figure 5e.** This result suggests that the increment in conductance is linked to the spin transition, only reversible by introducing water back in the MOF.

Finally, to probe the directionality of the conductivity in the crystal, additional electron transport measurements were carried out along the c-axis direction, that is, along the 1D Fe(II)-tetrazole chains (see **Figure 1c**) for sample **1**. **Figure S16†** shows the *IV* characteristics measured on the same crystal along the c-axis and in the *ab* plane. The current measured along the c-axis is 1-2 orders of magnitude lower than that measured in the *ab* plane. The conductance through the crystals seems to be highly anisotropic. This result is roughly reproducible in all the measured crystals. Addi
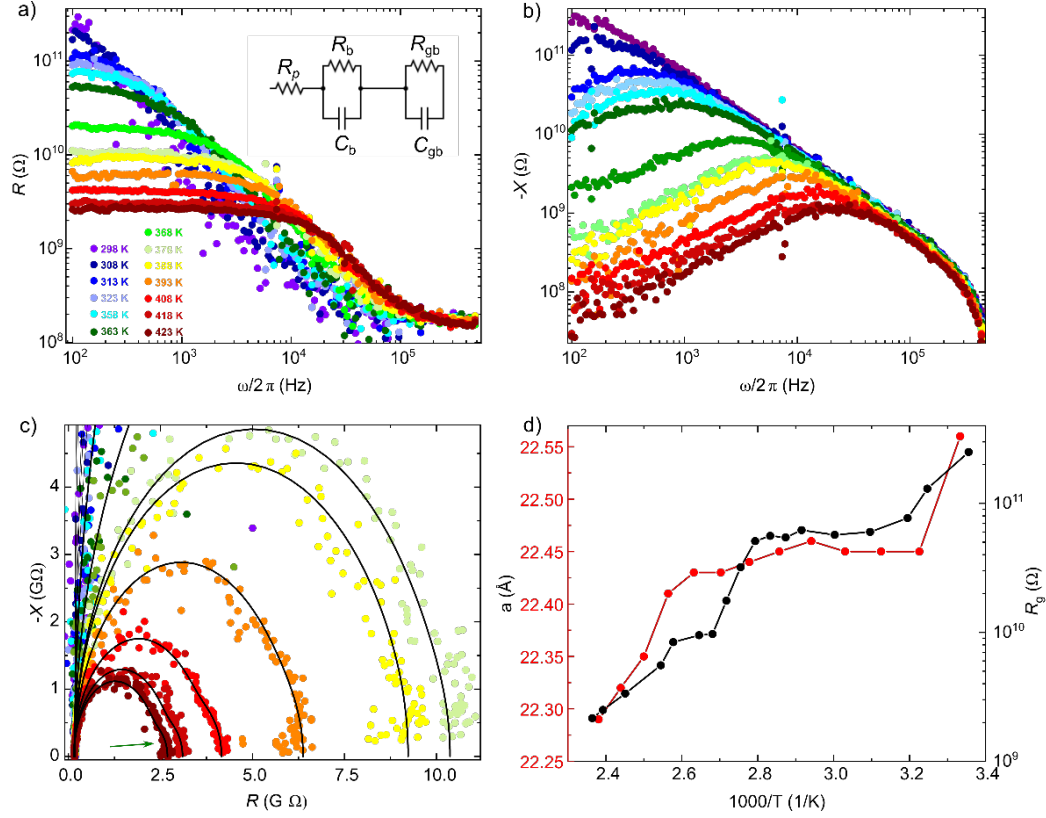
Figure 6. (a) Resistance R and (b) reactance X components of the complex impedance Z* measured as a function of the frequency and at different temperatures. The inset shows the equivalent electric circuit describing bulk (R_b, C_b), grain boundaries (R_{gb}, C_{gb}) contributions and contacts to the probes (R_p). (c) Nyquist representation of Z*. The solid lines are simulations of X and R using the equivalent circuit shown in (a). The green arrow marks the semicircle corresponding to the grain boundaries contribution. (d) R_b obtained from the fit to the Nyquist plots. R_b decreases with increasing temperature and qualitative follows the drop in the *a*, *b* lattice parameters.

AC impedance spectroscopy has been performed at different temperatures to gain a deeper insight into the different mechanisms (grain size, dielectric properties, grain boundaries, etc.) contributing to charge transport. The AC measurements are focused on the *ab* plane that presents the highest conductance.

Figure 6a,b show the real (resistance, *R*) and imaginary (reactance, *X*) components of the complex impedance *Z** measured in a **1** single crystal as a function of the frequency (5 Hz < $\omega/2\pi$ < 510 kHz) at different temperatures. The frequency dependence of *X* and *R* is indicative of capacitive effects in the sample, related either with its dielectric properties or with grain boundaries. **Figure 6c** shows the corresponding Nyquist representation of *Z** for high temperatures (See **Figure S17**† for the full plot and **Figure S19**† for the Debye relaxation time, τ, versus temperature, T). A large full semicircle appears accompanied by a significantly smaller semicircle overlapping at low frequencies (marked by the green arrow). This frequency response is typical for MOFs and other polycrystalline semiconductors.[74–76] The double semicircle can be modeled with an equivalent circuit made by two parallel RC circuits connected in series (inset in **Figure 6a**) accounting for two contributions to transport: the crystal grain or bulk (R_b, C_b) and the grain boundaries (R_{gb}, C_{gb}). An additional resistance R_p accounts for the contacts to the probes. Note that the main semicircle presents a nearly constant radius with no significant depression in the vertical axis. This is an indication of a Debye-like single conduction mechanism with a single relaxation rate, pointing to a high-quality crystallinity of the samples. Importantly, this single relaxation mode is essentially maintained after heating the samples over the structural transitions and up to 423 K. The crystallinity is preserved as observed in the single crystal X-ray diffraction experiments.

The solid lines in **Figure 6c** are fits to *R* and *X* obtained with the equivalent circuit shown in the inset on **Figure 6a** (See SI for the mathematical description of the model). **Figure 6d** shows the bulk resistance R_b as a function of the temperature obtained from the corresponding fits. R_b decreases with increasing temperature and qualitatively reproduces the drop in the *a,b* lattice

parameters length (red dots in **Figure 6d**). On the other hand, the bulk capacitance C_b remains approximately constant with temperature. A similar drop in resistance is observed for the grain boundaries (**Figure S18†**). Note however that the semicircle corresponding to the grain boundaries is almost completely overshadowed by the large one corresponding to the bulk. Therefore, the large uncertainty to obtain R_{gb} and C_{gb}, precludes us from establishing conclusions with respect to the grain boundaries. The change in conductance seems driven by a variation in the resistive properties of the crystal grain and not by changes in the dielectric properties. This trend is consistent with the intrinsic variation (contraction) of the lattice parameters with increasing temperature.

Electronic structure of 1 and 3

To gain knowledge about the experimental anisotropic conductivity and to rationalize the conductivity behavior of the different crystalline magneto-structural phases, density-functional theory (DFT) calculations were performed for **1** and **3.** In both cases, the calculations were performed using the periodic three-dimensional structure (see **ESI†** for further details) optimized starting from the experimental atomic coordinates. The projected band structure, the projected density of states and the plot of the valence band maximum (VBM) are reported in **Figure 7**.

For **3**, the valence band maximum (VBM) exhibits Fe character while the conduction band minimum (CBM) is mostly localized on the ligands as shown in the projected band structure and projected density of states in **Figure 7a**. In accordance with the ligand field splitting diagram, the VBM consists of a d-π* hybridized band between Fe and the whole π* state of the ligand. This band exhibits an *on-plane* character and spatially localizes along the *c*-axis (**Figure 7c**).

Specifically, each Fe atom hybridizes with two ligands along the same direction in the *ab* plane and every ligand hybridizes with two Fe atoms on each side (**Figure S22**†). The CBM and the CBM+1 are mostly localized on the ligands with a marginal contribution from the Fe atoms. These rather flat bands shown in **Figure 7a** are localized each along one specific direction.

The scenario is substantially modified in **1.** The VBM is a spin down state localized only on the HS Fe centers which exhibits negligible overlap with neighboring ligands and consequently negligible band dispersion as shown in **Figure 7b**, **7d**, and **Figure S26**†. The lower bands found at similar energy for spin up and spin down consist of d-π* hybridized states similar to the VBM of **3**, *i.e.* they localize on Fe and ligands along one specific direction within the *ab* plane. But because in this case they extend only on LS Fe, the hybridization along the *c*-direction occurs in a stepwise way as shown in **Figure 7d**. The four unoccupied bands at around 1.7 eV consist of π states of the ligand with marginal contribution from the Fe, similar to **3**.

To summarize, in **3**, the VBM is a Fe-ligand hybridized state that runs across the ab plane and connects all ligands along the c direction through two concomitant Fe atoms. In **1**, the Fe-ligand hybridization occurs through the same plane but the "on plane" character is lost since only the LS state iron participates in the hybridization, thus preventing a direct channel across the *c* direction. This scenario supports the higher conductance in the *ab* plane in **1** where the charge carriers can find a percolative path across the ab plane, in contrast with the *c*-axis direction. In addition, the analysis of the frontier bands suggests a more efficient channel for electron transport in **3** that would support a lowering of the activation barrier when switching from HS to LS with temperature. In addition, the presence of water in the unit cell of **3** negligibly affects the electronic structure near the Fermi level, as shown in **Figure S26**†. This result, together with the

analysis of the spatial localization of the electronic bands in **1** and **3**, reinforces the idea that the modulation of the conducting properties here presented are associated to a change in the spin state of the MOF.
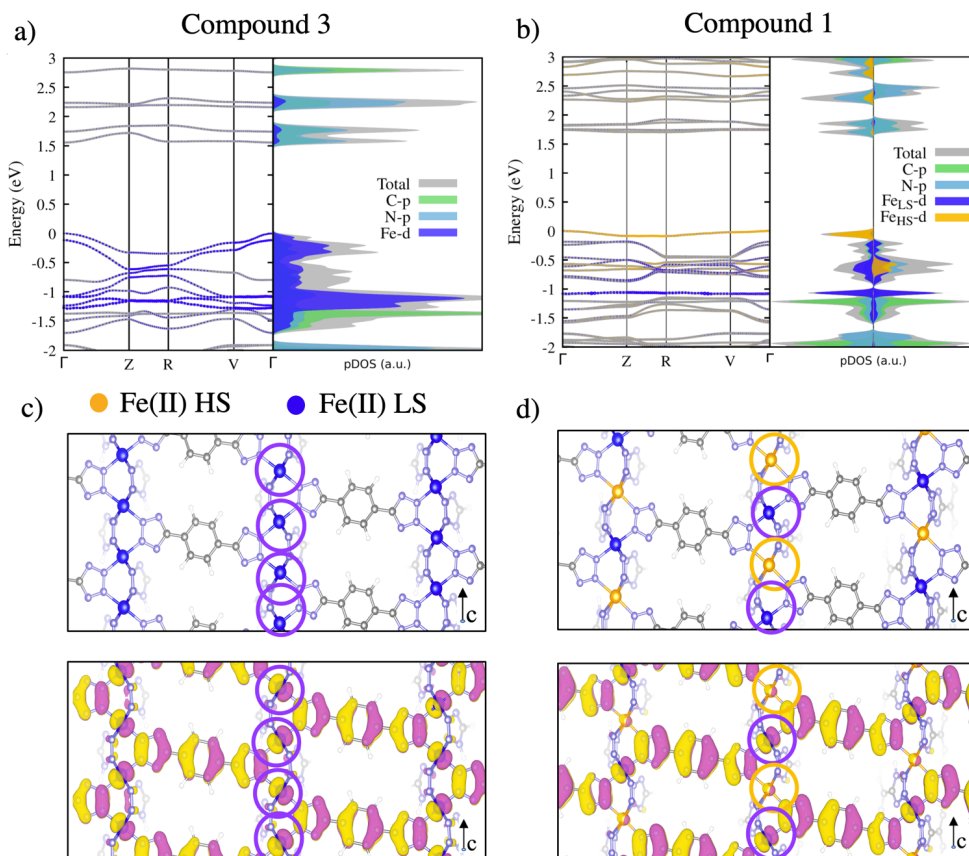

Figure 7. (a) Projected band structure and projected density of states computed using PBE+U for **3.** The size of the blue circles in the band structure indicates the magnitude of the weight of the Fe-d character at each k-point. (b) Projected band structure and projected density of states computed using PBE+U for **1.** The size of the blue and orange circles in the band structure indicates the magnitude of the weight of the Fe-d character for the spin down and spin up channels, respectively, at each k-point.(c)Side view of the optimized structure and isosurface of the wavefunction corresponding to the valence band maximum (VBM) at the Γ point. (d) Optimized structure and isosurface of the wavefunction

corresponding to the VBM-1 at the Γ point. Purple and orange circles in (c) and (d) indicate the position of the LS and HS Fe(II) ions respectively.

CONCLUSION

This work shows a detailed study of the physicochemical, electrical, magnetic and structural properties of a MOF that undergoes a reversible spin transition with temperature and concomitant loss of its host water molecules. Throughout the study, a structure-property correlation was carried out, which is fundamental for understanding the intrinsic properties of this material. In particular, a detailed single crystal to single crystal study in temperature was performed. The physico-chemical study showed that the sharp temperature-induced structural transitions in the crystals are accompanied by a change in colour (from orange to dark blue), volume (15 %) and magnetism (from paramagnetic to diamagnetic). These properties are restored when the porous material returns to its original composition, i.e. by incorporating water molecules in a controlled manner, in agreement with a reversible behavior.

In addition, electrical transport measurements through single crystals shows a modulation of the current at the temperature-induced spin transition, being the LS state more conducting than the HS state. Besides the conductance is highly anisotropic with respect to the axes of the crystal. To understand this result, a DFT study was carried out, which agrees with the idea that the diamagnetic iron spin state (LS) enhances electron transport in the 3D material (**Figure 8**). The investigation presented here provides a new scenario for the design and development of multifunctional 3D structures based on conductive molecules.
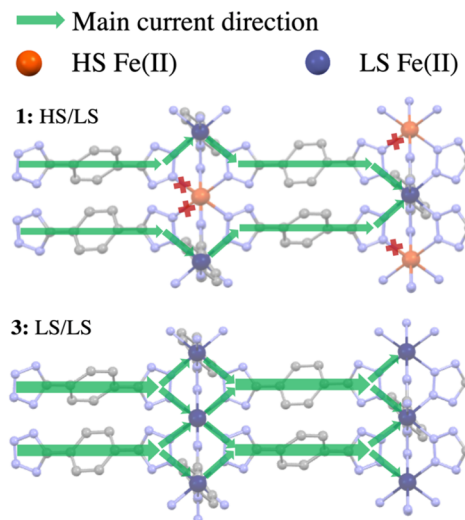
Figure 8. Schematic illustration of the proposed current path inside the SCO MOF for **1** (HS/LS) and **3**(LS/LS).

ASSOCIATED CONTENT

Supporting Information. Experimental section, synthesis of H_2bdt ligand and compounds **1**, **2** and **3**, infrared spectra of **1**, **2** and **3**, crystal data, structural refinement and selected distances, thermogravimetric analysis (TGA), optical reflectivity (O.R.), crystal size variation, powder X-ray diffraction (PXRD), representative *IV* curves, comparison between the *IV* curves of plane *ab* and *c* axis, additional measurements on the complex admittance and additional density functional theory calculations (DFT) (PDF).

AUTHOR INFORMATION

Corresponding Author

José Sánchez Costa - *IMDEA Nanociencia, C/ Faraday 9, Ciudad Universitaria de Cantoblanco, 28049 Madrid, Spain;* https://orcid.org/0000-0001-5426-7956*; Email:* jose.sanchezcosta@imdea.org

Enrique Burzurí - *IMDEA Nanociencia, C/ Faraday 9, Ciudad Universitaria de Cantoblanco, 28049 Madrid, Spain and Departamento de Física de la Materia Condensada and Condensed Matter Physics Center (IFIMAC), Universidad Autónoma de Madrid, 28049 Madrid, Spain*; *https://orcid.org/0000-0001-7906-7192; Email: enrique.burzuri@imdea.org*

Author Contributions

E.B. and J.S.C. conceived and designed experiments. A. M. and L. P. synthesized and crystallized compound **1**. A. M. and E. R. performed the electrical measurements. D. M. and J. A. performed the powder X-Ray diffraction experiments, A. L. M., A. F. B. and J.A.R.V. carried out the physico-chemical characterization. J. A. R. V. and E. C. S. measured and refined the crystal structure. A. F. B., A. L. M. and R. P. performed the theoretical study. R. P., E. B. and J. S.C. supervised research and directed data analysis. A. M., E. B. and J. S. C. wrote the manuscript, with contributions from all authors.

Funding Sources

REFERENCES

(1)   Furukawa, H.; Cordova, K. E.; O'Keeffe, M.; Yaghi, O. M. The Chemistry and Applications of Metal-Organic Frameworks. *Science* **2013**, *341* (6149), 1230444.

(2)   Kaye, S. S.; Dailly, A.; Yaghi, O. M.; Long, J. R. Impact of Preparation and Handling on the Hydrogen Storage Properties of $Zn_4O(1,4\text{-Benzenedicarboxylate})_3$ (MOF-5). *J. Am. Chem. Soc.* **2007**, *129* (46), 14176–14177.

(3)   Xie, L. S.; Skorupskii, G.; Dincă, M. Electrically Conductive Metal–Organic Frameworks. *Chem. Rev.* **2020**, *120* (16), 8536–8580.

(4)   Rubio-Giménez, V.; Tatay, S.; Martí-Gastaldo, C. Electrical Conductivity and Magnetic Bistability in Metal–Organic Frameworks and Coordination Polymers: Charge Transport and Spin Crossover at the Nanoscale. *Chem. Soc. Rev.* **2020**, *49* (15), 5601–5638.

(5)   Zhang, G.; Jin, L.; Zhang, R.; Bai, Y.; Zhu, R.; Pang, H. Recent Advances in the Development of Electronically and Ionically Conductive Metal-Organic Frameworks. *Coord. Chem. Rev.* **2021**, *439*, 213915.

(6)   Dou, J.-H.; Arguilla, M. Q.; Luo, Y.; Li, J.; Zhang, W.; Sun, L.; Mancuso, J. L.; Yang, L.; Chen, T.; Parent, L. R.; Skorupskii, G.; Libretto, N. J.; Sun, C.; Yang, M. C.; Dip, P. V.; Brignole, E. J.; Miller, J. T.; Kong, J.; Hendon, C. H.; Sun, J.; Dincă, M. Atomically Precise Single-Crystal Structures of Electrically Conducting 2D Metal–Organic Frameworks. *Nat. Mater.* **2021**, *20* (2), 222–228.

(7)   Ziebel, M. E.; Darago, L. E.; Long, J. R. Control of Electronic Structure and Conductivity in Two-Dimensional Metal–Semiquinoid Frameworks of Titanium, Vanadium, and Chromium. *J. Am. Chem. Soc.* **2018**, *140* (8), 3040–3051.

(8)   Avendano, C.; Zhang, Z.; Ota, A.; Zhao, H.; Dunbar, K. R. Dramatically Different Conductivity Properties of Metal-Organic Framework Polymorphs of Tl(TCNQ): An Unexpected Room-Temperature Crystal-to-Crystal Phase Transition. *Angew. Chem. Int. Ed.* **2011**, *50* (29), 6543–6547.

(9)   Huang, X.; Sheng, P.; Tu, Z.; Zhang, F.; Wang, J.; Geng, H.; Zou, Y.; Di, C.; Yi, Y.; Sun, Y.; Xu, W.; Zhu, D. A Two-Dimensional π–d Conjugated Coordination Polymer with Extremely High Electrical Conductivity and Ambipolar Transport Behaviour. *Nat. Commun.* **2015**, *6* (1), 7408.

(10)   Sheberla, D.; Sun, L.; Blood-Forsythe, M. A.; Er, S.; Wade, C. R.; Brozek, C. K.; Aspuru-Guzik, A.; Dincă, M. High Electrical Conductivity in Ni_3(2,3,6,7,10,11-Hexaiminotriphenylene)$_2$, a Semiconducting Metal–Organic Graphene Analogue. *J. Am. Chem. Soc.* **2014**, *136* (25), 8859–8862.

(11)   Campbell, M. G.; Sheberla, D.; Liu, S. F.; Swager, T. M.; Dincă, M. Cu_3(Hexaiminotriphenylene)$_2$: An Electrically Conductive 2D Metal-Organic Framework for Chemiresistive Sensing. *Angew. Chem. Int. Ed.* **2015**, *54* (14), 4349–4352.

(12)   Zeng, M.-H.; Wang, Q.-X.; Tan, Y.-X.; Hu, S.; Zhao, H.-X.; Long, L.-S.; Kurmoo, M. Rigid Pillars and Double Walls in a Porous Metal-Organic Framework: Single-Crystal to Single-Crystal, Controlled Uptake and Release of Iodine and Electrical Conductivity. *J. Am. Chem. Soc.* **2010**, *132* (8), 2561–2563.

(13)   Aubrey, M. L.; Wiers, B. M.; Andrews, S. C.; Sakurai, T.; Reyes-Lillo, S. E.; Hamed, S. M.; Yu, C.-J.; Darago, L. E.; Mason, J. A.; Baeg, J.-O.; Grandjean, F.; Long, G. J.; Seki, S.; Neaton, J. B.; Yang, P.; Long, J. R. Electron Delocalization and Charge Mobility as a Function of Reduction in a Metal–Organic Framework. *Nat. Mater* **2018**, *17* (7), 625–632.

(14)   Talin, A. A.; Centrone, A.; Ford, A. C.; Foster, M. E.; Stavila, V.; Haney, P.; Kinney, R. A.; Szalai, V.; El Gabaly, F.; Yoon, H. P.; Léonard, F.; Allendorf, M. D. Tunable Electrical Conductivity in Metal-Organic Framework Thin-Film Devices. *Science* **2014**, *343* (6166), 66–69.

(15)   Sun, L.; Hendon, C. H.; Park, S. S.; Tulchinsky, Y.; Wan, R.; Wang, F.; Walsh, A.; Dincă, M. Is Iron Unique in Promoting Electrical Conductivity in MOFs? *Chem. Sci.* **2017**, *8* (6), 4450–4457.

(16)   Sun, L.; Hendon, C. H.; Minier, M. A.; Walsh, A.; Dincă, M. Million-Fold Electrical Conductivity Enhancement in Fe_2(DEBDC) versus Mn_2(DEBDC) (E = S, O). *J. Am. Chem. Soc.* **2015**, *137* (19), 6164–6167.

(17)   Mínguez Espallargas, G.; Coronado, E. Magnetic Functionalities in MOFs: From the Framework to the Pore. *Chem. Soc. Rev.* **2018**, *47* (2), 533–557.

(18)   Coronado, E. Molecular Magnetism: From Chemical Design to Spin Control in Molecules, Materials and Devices. *Nat. Rev. Mater.* **2020**, *5* (2), 87–104.

(19)   Reed, D. A.; Xiao, D. J.; Gonzalez, M. I.; Darago, L. E.; Herm, Z. R.; Grandjean, F.; Long, J. R. Reversible CO Scavenging via Adsorbate-Dependent Spin State Transitions in an Iron(II)–Triazolate Metal–Organic Framework. *J. Am. Chem. Soc.* **2016**, *138* (17), 5594–5602.

(20)   Shiga, T.; Saiki, R.; Akiyama, L.; Kumai, R.; Natke, D.; Renz, F.; Cameron, J. M.; Newton, G. N.; Oshio, H. A Brønsted-Ligand-Based Iron Complex as a Molecular Switch with Five Accessible States. *Angew. Chem. Int. Ed.* **2019**, *58* (17), 5658–5662.

(21)   Rodríguez-Jiménez, S.; Feltham, H. L. C.; Brooker, S. Non-Porous Iron(II)-Based Sensor: Crystallographic Insights into a Cycle of Colorful Guest-Induced Topotactic Transformations. *Angew. Chem. Int. Ed.* **2016**, *55* (48), 15067–15071.

(22)   León-Alcaide, L.; López-Cabrelles, J.; Mínguez Espallargas, G.; Coronado, E. 2D Magnetic MOFs with Micron-Lateral Size by Liquid Exfoliation. *Chem. Commun.* **2020**, *56* (55), 7657–7660.

(23)   López-Cabrelles, J.; Mañas-Valero, S.; Vitórica-Yrezábal, I. J.; Šiškins, M.; Lee, M.; Steeneken, P. G.; van der Zant, H. S. J.; Mínguez Espallargas, G.; Coronado, E. Chemical Design and Magnetic Ordering in Thin Layers of 2D Metal–Organic Frameworks (MOFs). *J. Am. Chem. Soc.* **2021**, *143* (44), 18502–18510.

(24)   González, J.; Sevilla, P.; Gabarró-Riera, G.; Jover, J.; Echeverría, J.; Fuertes, S.; Arauzo, A.; Bartolomé, E.; Sañudo, E. C. A Multifunctional Dysprosium-Carboxylato 2D Metal–Organic Framework. *Angew. Chem. Int. Ed.* **2021**, *60* (21), 12001–12006.

(25)   Chen, M.; Sañudo, E. C.; Jiménez, E.; Fang, S.-M.; Liu, C.-S.; Du, M. Lanthanide–Organic Coordination Frameworks Showing New 5-Connected Network Topology and 3D Ordered Array of Single-Molecular Magnet Behavior in the Dy Case. *Inorg. Chem.* **2014**, *53* (13), 6708–6714.

(26)   Orts-Arroyo, M.; Rabelo, R.; Carrasco-Berlanga, A.; Moliner, N.; Cano, J.; Julve, M.; Lloret, F.; De Munno, G.; Ruiz-García, R.; Mayans, J.; Martínez-Lillo, J.; Castro, I. Field-Induced Slow Magnetic Relaxation and Magnetocaloric Effects in an Oxalato-Bridged Gadolinium(III)-Based 2D MOF. *Dalton Trans.* **2021**, *50* (11), 3801–3805.

(27)   Dong, R.; Zhang, Z.; Tranca, D. C.; Zhou, S.; Wang, M.; Adler, P.; Liao, Z.; Liu, F.; Sun, Y.; Shi, W.; Zhang, Z.; Zschech, E.; Mannsfeld, S. C. B.; Felser, C.; Feng, X. A Coronene-Based

Semiconducting Two-Dimensional Metal-Organic Framework with Ferromagnetic Behavior. *Nat. Commun.* **2018**, *9* (1), 2637.

(28)   Lian, K.-T.; Wu, W.-W.; Huang, G.-Z.; Liu, Y.; Wu, S.-G.; Ni, Z.-P.; Tong, M.-L. Reversible Step Spin Crossover Modulation *via* Water Absorption and Dehydration in a 3D Hofmann-Type Framework. *Inorg. Chem. Front.* **2021**, *8* (19), 4334–4340.

(29)   Piñeiro-López, L.; Valverde-Muñoz, F.-J.; Trzop, E.; Muñoz, M. C.; Seredyuk, M.; Castells-Gil, J.; da Silva, I.; Martí-Gastaldo, C.; Collet, E.; Real, J. A. Guest Induced Reversible on–off Switching of Elastic Frustration in a 3D Spin Crossover Coordination Polymer with Room Temperature Hysteretic Behaviour. *Chem. Sci.* **2021**, *12* (4), 1317–1326.

(30)   Molnár, G.; Rat, S.; Salmon, L.; Nicolazzi, W.; Bousseksou, A. Spin Crossover Nanomaterials: From Fundamental Concepts to Devices. *Adv. Mater.* **2018**, *30* (5), 1703862.

(31)   Garcia, Y.; Niel, V.; Muñoz, M. C.; Real, J. A. Spin Crossover in 1D, 2D and 3D Polymeric Fe(II) Networks. In *Spin Crossover in Transition Metal Compounds I*; Gütlich, P., Goodwin, H. A., Eds.; Topics in Current Chemistry; Springer Berlin Heidelberg: Berlin, Heidelberg, **2004**; Vol. 233, pp 229–257.

(32)   Brooker, S. Spin Crossover with Thermal Hysteresis: Practicalities and Lessons Learnt. *Chem. Soc. Rev.* **2015**, *44* (10), 2880–2892.

(33)   Sanchez Costa, J. Macroscopic Methods: Magnetic, Optical, and Calorimetric Techniques. *C. R. Chim.* **2018**, *21* (12), 1121–1132.

(34)   Bonhommeau, S.; Guillon, T.; Lawson Daku, L. M.; Demont, P.; Sanchez Costa, J.; Létard, J.-F.; Molnár, G.; Bousseksou, A. Photoswitching of the Dielectric Constant of the Spin-Crossover Complex [Fe(L)(CN)$_2$]·H$_2$O. *Angew. Chem. Int. Ed.* **2006**, *45* (10), 1625–1629.

(35)   Bousseksou, A.; Varret, F.; Goiran, M.; Boukheddaden, K.; Tuchagues, J. P. The Spin Crossover Phenomenon Under High Magnetic Field. In *Spin Crossover in Transition Metal Compounds III*; Topics in Current Chemistry; Springer Berlin Heidelberg: Berlin, Heidelberg, **2004**; Vol. 235, pp 65–84.

(36)   Li, B.; Wei, R.-J.; Tao, J.; Huang, R.-B.; Zheng, L.-S.; Zheng, Z. Solvent-Induced Transformation of Single Crystals of a Spin-Crossover (SCO) Compound to Single Crystals with Two Distinct SCO Centers. *J. Am. Chem. Soc.* **2010**, *132* (5), 1558–1566.

(37)   Bartual-Murgui, C.; Salmon, L.; Akou, A.; Ortega-Villar, N. A.; Shepherd, H. J.; Muñoz, M. C.; Molnár, G.; Real, J. A.; Bousseksou, A. Synergetic Effect of Host-Guest Chemistry and Spin Crossover in 3D Hofmann-like Metal-Organic Frameworks [Fe(Bpac)M(CN)$_4$] (M=Pt, Pd, Ni). *Chem. Eur. J.* **2012**, *18* (2), 507–516.

(38)   Bao, X.; Shepherd, H. J.; Salmon, L.; Molnár, G.; Tong, M.-L.; Bousseksou, A. The Effect of an Active Guest on the Spin Crossover Phenomenon. *Angew. Chem. Int. Ed.* **2013**, *52* (4), 1198–1202.

(39)   Senthil Kumar, K.; Ruben, M. Emerging Trends in Spin Crossover (SCO) Based Functional Materials and Devices. *Coord. Chem. Rev.* **2017**, *346*, 176–205.

(40)   Koo, Y.-S.; Galán-Mascarós, J. R. Spin Crossover Probes Confer Multistability to Organic Conducting Polymers. *Adv. Mater.* **2014**, *26* (39), 6785–6789.

(41)   Boix-Constant, C.; García-López, V.; Navarro-Moratalla, E.; Clemente-León, M.; Zafra, J. L.; Casado, J.; Guinea, F.; Mañas-Valero, S.; Coronado, E. Strain Switching in van Der Waals Heterostructures Triggered by a Spin-Crossover Metal–Organic Framework. *Adv. Mater.* **2022**, *34* (11), 2110027.

(42)   Prins, F.; Monrabal-Capilla, M.; Osorio, E. A.; Coronado, E.; van der Zant, H. S. J. Room-Temperature Electrical Addressing of a Bistable Spin-Crossover Molecular System. *Adv. Mater.* **2011**, *23* (13), 1545–1549.

(43)   Villalva, J.; Develioglu, A.; Montenegro-Pohlhammer, N.; Sánchez-de-Armas, R.; Gamonal, A.; Rial, E.; García-Hernández, M.; Ruiz-Gonzalez, L.; Sanchez Costa, J.; Calzado, C. J.; Pérez, E. M.; Burzurí, E. Spin-State-Dependent Electrical Conductivity in Single-Walled Carbon Nanotubes Encapsulating Spin-Crossover Molecules. *Nat. Commun.* **2021**, *12* (1), 1578.

(44)   Burzurí, E.; García-Fuente, A.; García-Suárez, V.; Senthil Kumar, K.; Ruben, M.; Ferrer, J.; van der Zant, H. S. J. Spin-State Dependent Conductance Switching in Single Molecule-Graphene Junctions. *Nanoscale* **2018**, *10* (17), 7905–7911.

(45)   Lefter, C.; Davesne, V.; Salmon, L.; Molnár, G.; Demont, P.; Rotaru, A.; Bousseksou, A. Charge Transport and Electrical Properties of Spin Crossover Materials: Towards Nanoelectronic and Spintronic Devices. *Magnetochemistry* **2016**, *2* (1), 18.

(46)   Dayen, J.-F.; Konstantinov, N.; Palluel, M.; Daro, N.; Kundys, B.; Soliman, M.; Chastanet, G.; Doudin, B. Room Temperature Optoelectronic Devices Operating with Spin Crossover Nanoparticles. *Mater. Horiz.* **2021**, *8* (8), 2310–2315.

(47)   Senthil Kumar, K.; Šalitroš, I.; Boubegtiten-Fezoua, Z.; Moldovan, S.; Hellwig, P.; Ruben, M. A Spin Crossover (SCO) Active Graphene-Iron(II) Complex Hybrid Material. *Dalton Trans.* **2018**, *47* (1), 35–40.

(48)   Djukic, B.; Lemaire, M. T. Hybrid Spin-Crossover Conductor Exhibiting Unusual Variable-Temperature Electrical Conductivity. *Inorg. Chem.* **2009**, *48* (22), 10489–10491.

(49)   Rotaru, A.; Gural'skiy, I. A.; Molnár, G.; Salmon, L.; Demont, P.; Bousseksou, A. Spin State Dependence of Electrical Conductivity of Spin Crossover Materials. *Chem. Commun.* **2012**, *48* (35), 4163–4165.

(50)   Shi, S.; Schmerber, G.; Arabski, J.; Beaufrand, J.-B.; Kim, D. J.; Boukari, S.; Bowen, M.; Kemp, N. T.; Viart, N.; Rogez, G.; Beaurepaire, E.; Aubriet, H.; Petersen, J.; Becker, C.; Ruch, D. Study of Molecular Spin-Crossover Complex Fe(Phen)2(NCS)2 Thin Films. *Appl. Phys. Lett.* **2009**, *95* (4), 043303.

(51)   Rotaru, A.; Dugay, J.; Tan, R. P.; Guralskiy, I. A.; Salmon, L.; Demont, P.; Carrey, J.; Molnár, G.; Respaud, M.; Bousseksou, A. Nano-Electromanipulation of Spin Crossover Nanorods: Towards Switchable Nanoelectronic Devices. *Adv. Mater.* **2013**, *25* (12), 1745–1749.

(52)   Ishikawa, R.; Ueno, S.; Nifuku, S.; Horii, Y.; Iguchi, H.; Miyazaki, Y.; Nakano, M.; Hayami, S.; Kumagai, S.; Katoh, K.; Li, Z.; Yamashita, M.; Kawata, S. Simultaneous Spin-

Crossover Transition and Conductivity Switching in a Dinuclear Iron(II) Coordination Compound Based on 7,7′,8,8′-Tetracyano- *p* -quinodimethane. *Chem. Eur. J.* **2020**, *26* (6), 1278–1285.

(53)   Wang, H.; Ge, J.; Hua, C.; Jiao, C.; Wu, Y.; Leong, C. F.; D'Alessandro, D. M.; Liu, T.; Zuo, J. Photo- and Electronically Switchable Spin-Crossover Iron(II) Metal–Organic Frameworks Based on a Tetrathiafulvalene Ligand. *Angew. Chem. Int. Ed.* **2017**, *56* (20), 5465–5470.

(54)   Phan, H.; Benjamin, S. M.; Steven, E.; Brooks, J. S.; Shatruk, M. Photomagnetic Response in Highly Conductive Iron(II) Spin-Crossover Complexes with TCNQ Radicals. *Angew. Chem.* **2015**, *127* (3), 837–841.

(55)   Takahashi, K.; Cui, H.-B.; Okano, Y.; Kobayashi, H.; Mori, H.; Tajima, H.; Einaga, Y.; Sato, O. Evidence of the Chemical Uniaxial Strain Effect on Electrical Conductivity in the Spin-Crossover Conducting Molecular System: [Fe ^{III}(Qnal)$_2$][Pd(Dmit)$_2$]$_5$ ·Acetone. *J. Am. Chem. Soc.* **2008**, *130* (21), 6688–6689.

(56)   Yan, Z.; Li, M.; Gao, H.-L.; Huang, X.-C.; Li, D. High-Spin versus Spin-Crossover versus Low-Spin: Geometry Intervention in Cooperativity in a 3D Polymorphic Iron(II)–Tetrazole MOFs System. *Chem. Commun.* **2012**, *48* (33), 3960.

(57)   Liu, W.-T.; Li, J.-Y.; Ni, Z.-P.; Bao, X.; Ou, Y.-C.; Leng, J.-D.; Liu, J.-L.; Tong, M.-L. Incomplete Spin Crossover versus Antiferromagnetic Behavior Exhibited in Three-Dimensional Porous Fe(II)-Bis(Tetrazolate) Frameworks. *Cryst. Growth Des.* **2012**, *12* (3), 1482–1488.

(58)   Xie, L. S.; Sun, L.; Wan, R.; Park, S. S.; DeGayner, J. A.; Hendon, C. H.; Dincă, M. Tunable Mixed-Valence Doping toward Record Electrical Conductivity in a Three-Dimensional Metal–Organic Framework. *J. Am. Chem. Soc.* **2018**, *140* (24), 7411–7414.

(59)   Demko, Z. P.; Sharpless, K. B. Preparation of 5-Substituted 1 *H* -Tetrazoles from Nitriles in Water. *J. Org. Chem.* **2001**, *66* (24), 7945–7950.

(60)   Giannozzi, P.; Andreussi, O.; Brumme, T.; Bunau, O.; Buongiorno Nardelli, M.; Calandra, M.; Car, R.; Cavazzoni, C.; Ceresoli, D.; Cococcioni, M.; Colonna, N.; Carnimeo, I.; Dal Corso, A.; de Gironcoli, S.; Delugas, P.; DiStasio, R. A.; Ferretti, A.; Floris, A.; Fratesi, G.; Fugallo, G.; Gebauer, R.; Gerstmann, U.; Giustino, F.; Gorni, T.; Jia, J.; Kawamura, M.; Ko, H.-Y.; Kokalj, A.; Küçükbenli, E.; Lazzeri, M.; Marsili, M.; Marzari, N.; Mauri, F.; Nguyen, N. L.; Nguyen, H.-V.; Otero-de-la-Roza, A.; Paulatto, L.; Poncé, S.; Rocca, D.; Sabatini, R.; Santra, B.; Schlipf, M.; Seitsonen, A. P.; Smogunov, A.; Timrov, I.; Thonhauser, T.; Umari, P.; Vast, N.; Wu, X.; Baroni, S. Advanced Capabilities for Materials Modelling with Quantum ESPRESSO. *J. Phys.: Condens. Matter.* **2017**, *29* (46), 465901.

(61)   Giannozzi, P.; Baseggio, O.; Bonfà, P.; Brunato, D.; Car, R.; Carnimeo, I.; Cavazzoni, C.; de Gironcoli, S.; Delugas, P.; Ferrari Ruffino, F.; Ferretti, A.; Marzari, N.; Timrov, I.; Urru, A.; Baroni, S. QUANTUM ESPRESSO toward the Exascale. *J. Chem. Phys.* **2020**, *152* (15), 154105.

(62)   Hamann, D. R. Optimized Norm-Conserving Vanderbilt Pseudopotentials. *Phys. Rev. B* **2013**, *88* (8), 085117.

(63)   Cococcioni, M.; de Gironcoli, S. Linear Response Approach to the Calculation of the Effective Interaction Parameters in the LDA + U Method. *Phys. Rev. B* **2005**, *71* (3), 035105.

(64)   Mariano, L. A.; Vlaisavljevich, B.; Poloni, R. Biased Spin-State Energetics of Fe(II) Molecular Complexes within Density-Functional Theory and the Linear-Response Hubbard *U* Correction. *J. Chem. Theory Comput.* **2020**, *16* (11), 6755–6762.

(65)   Mariano, L. A.; Vlaisavljevich, B.; Poloni, R. Improved Spin-State Energy Differences of Fe(II) Molecular and Crystalline Complexes *via* the Hubbard *U* -Corrected Density. *J. Chem. Theory Comput.* **2021**, *17* (5), 2807–2816.

(66)   Heyd, J.; Scuseria, G. E.; Ernzerhof, M. Hybrid Functionals Based on a Screened Coulomb Potential. *J. Chem. Phys.* **2003**, *118* (18), 8207–8215.

(67)   Peralta, J. E.; Heyd, J.; Scuseria, G. E.; Martin, R. L. Spin-Orbit Splittings and Energy Band Gaps Calculated with the Heyd-Scuseria-Ernzerhof Screened Hybrid Functional. *Phys. Rev. B* **2006**, *74* (7), 073101.

(68)   Sanchez Costa, J.; Rodríguez-Jiménez, S.; Craig, G. A.; Barth, B.; Beavers, C. M.; Teat, S. J.; Aromí, G. Three-Way Crystal-to-Crystal Reversible Transformation and Controlled Spin Switching by a Nonporous Molecular Material. *J. Am. Chem. Soc.* **2014**, *136* (10), 3869–3874.

(69)   Turo-Cortés, R.; Bartual-Murgui, C.; Castells-Gil, J.; Muñoz, M. C.; Martí-Gastaldo, C.; Real, J. A. Reversible Guest-Induced Gate-Opening with Multiplex Spin Crossover Responses in Two-Dimensional Hofmann Clathrates. *Chem. Sci.* **2020**, *11* (41), 11224–11234.

(70)   Piñeiro-López, L.; Seredyuk, M.; Muñoz, M. C.; Real, J. A. Effect of Guest Molecules on Spin Transition Temperature in Loaded Hofmann-Like Clathrates with Improved Porosity. *Eur. J. Inorg. Chem.* **2020**, *2020* (9), 764–769.

(71)   Chen, W.-B.; Chen, Y.-C.; Yang, M.; Tong, M.-L.; Dong, W. Water Molecule Induced Reversible Single-Crystal-to-Single-Crystal Transformation between Two Trinuclear Fe(ii) Complexes with Different Spin Crossover Behaviour. *Dalton Trans.* **2018**, *47* (12), 4307–4314.

(72)   Rodríguez-Velamazán, J. A.; González, M. A.; Real, J. A.; Castro, M.; Muñoz, M. C.; Gaspar, A. B.; Ohtani, R.; Ohba, M.; Yoneda, K.; Hijikata, Y.; Yanai, N.; Mizuno, M.; Ando, H.; Kitagawa, S. A Switchable Molecular Rotator: Neutron Spectroscopy Study on a Polymeric Spin-Crossover Compound. *J. Am. Chem. Soc.* **2012**, *134* (11), 5083–5089.

(73)   Sánchez-de-Armas, R.; Montenegro-Pohlhammer, N.; Develioglu, A.; Burzurí, E.; Calzado, C. J. Spin-Crossover Complexes in Nanoscale Devices: Main Ingredients of the Molecule–Substrate Interactions. *Nanoscale* **2021**, *13* (44), 18702–18713.

(74)   Develioglu, A.; Resines-Urien, E.; Poloni, R.; Martín-Pérez, L.; Sanchez Costa, J.; Burzurí, E. Tunable Proton Conductivity and Color in a Nonporous Coordination Polymer via Lattice Accommodation to Small Molecules. *Adv. Sci.* **2021**, *8* (22), 2102619.

(75)   Stankiewicz, J.; Tomás, M.; Dobrinovitch, I. T.; Forcén-Vázquez, E.; Falvello, L. R. Proton Conduction in a Nonporous One Dimensional Coordination Polymer. *Chem. Mater.* **2014**, *26* (18), 5282–5287.

(76)   Xue, W.; Deng, W.; Chen, H.; Liu, R.; Taylor, J. M.; Li, Y.; Wang, L.; Deng, Y.; Li, W.; Wen, Y.; Wang, G.; Wan, C.; Xu, G. MOF-Directed Synthesis of Crystalline Ionic Liquids with Enhanced Proton Conduction. *Angew. Chem. Int. Ed.* **2021**, *60* (3), 1290–1297.

Table of contents